OPTIMIZED EXEMPLAR-BASED LIGHT FIELD SUPER-RESOLUTION

BURHAN AYDENİZ

Thesis for the Master's Program in Electrical and Electronics Engineering

Graduate School

Izmir University of Economics

Izmir

2023

OPTIMIZED EXEMPLAR-BASED LIGHT FIELD SUPER-RESOLUTION

BURHAN AYDENİZ

THESIS ADVISOR: ASSOC. PROF. DR. MEHMET TÜRKAN

A Master's Thesis
Submitted to
the Graduate School of Izmir University of Economics
the Department of Electrical and Electronics Engineering

Izmir
2023

ETHICAL DECLARATION

I hereby declare that I am the sole author of this thesis and that I have conducted my work in accordance with academic rules and ethical behaviour at every stage from the planning of the thesis to its defence. I confirm that I have cited all ideas, information and findings that are not specific to my study, as required by the code of ethical behaviour, and that all statements not cited are my own.
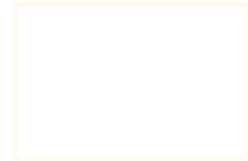
Name, Surname:

Burhan Aydeniz

Date:

01/02/2023

Signature:

ABSTRACT

OPTIMIZED EXEMPLAR-BASED LIGHT FIELD SUPER-RESOLUTION

Aydeniz, Burhan

Master's Program in Electrical and Electronics Engineering

Advisor: Assoc. Prof. Dr. Mehmet Türkan

January, 2023

The light field imaging technique can produce views captured from light rays in different locations and directions. Due to several hardware restrictions, light field images have low spatial resolution. By aiming to reconstruct image details, different high resolution images can be estimated in an image generation model. In literature, several super-resolution methods have been proposed to solve this ill-posed optimization problem. In this thesis, exemplar-based light field super-resolution algorithms have been developed by means of Linear Embeddings and Orthogonal Matching Pursuits through exemplar patch pairs extracted from low resolution images. The proposed method estimates high resolution images in low disparity light field datasets. According to statistical and visual results, the proposed exemplar-based light field super-resolution approach provides remarkable performance when compared to state-of-the-art algorithms.

Keywords: light field, super-resolution, exemplar-based, linear embedding, orthogonal matching pursuit

ÖZET

OPTİMİZE EDİLMİŞ ÖRNEK-TABANLI IŞIK ALAN SÜPER-ÇÖZÜNÜRLÜK

Aydeniz, Burhan

Elektrik ve Elektronik Mühendisliği Yüksek Lisans Programı

Tez Danışmanı: Doç. Dr. Mehmet Türkan

Ocak, 2023

Işık alanı görüntüleme tekniği, farklı konumlarda ve yönlerde yakalanan ışık hüzmelerinin görüntülerini üretebilir. Çeşitli donanım kısıtlamaları nedeniyle, ışık alanı görüntüleri düşük uzamsal çözünürlüğe sahiptir. Görüntü üretim modelinde, görüntü detaylarının korunması amacıyla, farklı yüksek çözünürlüklü görüntüler tahmin edilebilir. Bu kötü konumlanmış optimizasyon problemini çözmek için literatürde bir cok süper-çözünürlük yöntemi önerilmiştir. Bu tezde, düşük çözünürlüklü görüntülerden çıkarılan örnek yama çiftleri aracılığıyla doğrusal yerleştirme ve dikgen eşleştirme takibi tabanlı algoritmalar kullanılarak örnek tabanlı ışık alanı süper-çözünürlük algoritmaları geliştirilmiştir. Önerilen yöntemler, düşük eşitsizlikli ışık alanı verisetlerinde yüksek çözünürlüklü görüntüleri tahmin etmektedir. İstatistiksel ve görsel sonuçlara göre, en ileri teknoloji algoritmalar ile karşılaştırıldığında önerilen örnek tabanlı ışık alanı süper çözünürlük yaklaşımı dikkate değer bir performans sağlamaktadır.

Anahtar Kelimeler: ışık alan, süper çözünürlük, örnek tabanlı, doğrusal yerleştirme, dikgen eşleştirme takibi

ACKNOWLEDGEMENTS

TABLE OF CONTENTS

LIST OF TABLES

LIST OF FIGURES

LIST OF ABBREVIATIONS

2D: Two-dimensional

4D: Four-dimensional

5D: Five-dimensional

BP: Non-iterative Back-projection

CNN: Convolutional Neural Network

EDUMS: Edge Directed Unsharp Masking Sharpening

GAN: Generative Adversarial Network

GPU: Graphics Processing Unit

HR: High Resolution

IBP: Iterative Back-projection

IMsF: Implicity Multi-scale Fusion

K-NN: K-Nearest Neighbor

LF: Light Field

LLE: Locally Linear Embedding

LMMSE: Linear Minimum Mean Square Estimator

LR: Low Resolution

MeanSubs-OMP: Mean Substracted Orthogonal Matching Pursuit

NN: Neural Network

OMP: Orthogonal Matching Pursuit

OptLLE-LFSR: Optimized Locally Linear Embedding Based Nearest Neighbor Constraint Light Field Super-Resolution

OptMeanSubs-OMP-LFSR via SOM: Optimized Mean Substracted Orthogonal Matching Pursuit Algorithm Based Nearest Neighbor Constraint Light Field Super-Resolution via Deblurring with Self-Organizing Map

OptOMP-LFSR via EDUMS: Optimized Orthogonal Matching Pursuit Algorithm Based Nearest Neighbor Constraint Light Field Super-Resolution via Edge Directed Unsharp Masking Sharpening Method

OptOMP-LFSR via SOM: Optimized Orthogonal Matching Pursuit Algorithm Based Nearest Neighbor Constraint Light Field Super-Resolution via Deblurring with Self-Organizing Map

PCA: Principal Component Analysis

PSNR: Peak Signal-to-Noise Ratio

RR: Multivariate Ridge Regression

SAI: Sub-aperture Image

SISR: Single Image Super-Resolution

SOM: Self-Organizing Map

SR: Super-Resolution

TIP: Traditional Image Processing

CHAPTER 1: INTRODUCTION

Humanity has always wondered about making sense of environment and wanted to develop it further. Therefore, humanity has tried to figure the nature and its circumstances. These trials sometimes be photography, painting, or other kind of visual arts. Since the early age of the invention of photography, the working principles have been usually like a copy of human vision system. Fundamentally, the copied principle is that the light beam is refracted by the lens and projected onto the sensors. Thus, similar to human vision system, the object or the scene can be captured by imaging systems. With the principle, due to the inability to capture light rays from different angles and intensities, two-dimensional images with low depth perception are produced. However, as human beings always do, they solve this problem in a way that is inspired by living forms. As mentioned in the study of (Rodríguez-Gironés and Ruiz, 2016), many insects, spiders and flies have more than one lens, unlike the human vision system. In this way, these creatures can capture light beams with different angles and intensities. LF imaging also captures light beams in a similar way to this principle.

As it is shown in Figure 1, LF imaging technique is a technique that can capture light rays at different locations and different directions. In fact, different from 2D conventional imaging technique, the technique is able to detect the spatial and angular variations in the intensity of light rays (Adelson and Bergen, 2020). Thanks to the microlens array, which is frequently preferred in LF imaging, these variations can be captured in different parts of the sensor. As it is known, an LF can be formulated as a 4D function that represents the spatial distribution, and the angular distribution of light rays. To comprehend 4D LF matrix views (see Figure 1), the represented spatial dimensions as a 2D matrix is also called SAI, these SAIs constitute the 4D matrix with the appropriate angular dimension locations. Thus, when each SAI in the 4D matrix is examined, it can be observed that each of the others shifts by a certain amount of pixels.
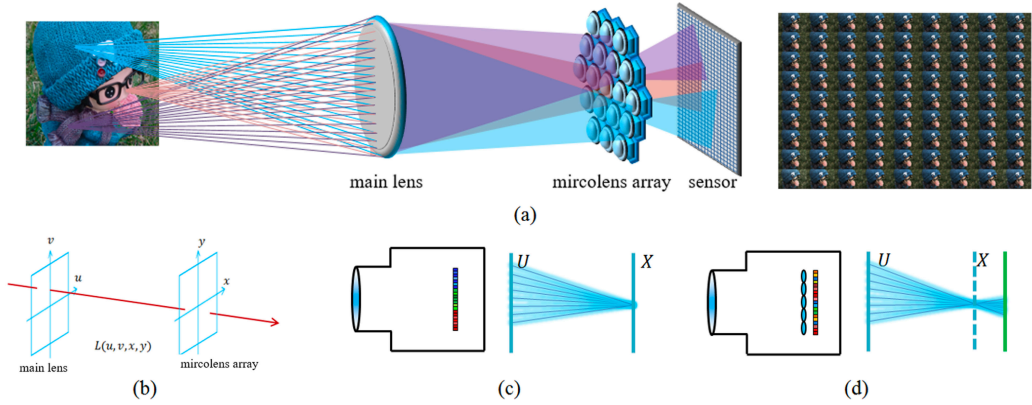
Figure 1. LF Imaging: (a) Structure of a microlens-based LF camera. (b) Two-plane parameterization model. (c) Basic structure of conventional cameras. (d) Basic structure of microlens-based LF camera. (Source: Wang et al., 2018)

To enhance the captured scene, this technique presents images those enable some benefits such as post-capture refocusing, controlling and extended depth-of-field, different viewpoint rendering. Therefore, as mentioned in (Ng Ren, 2006), these capabilities can be employed for image or video post-production and virtual or augmented reality applications. Despite all these favorable features, LF imaging systems have some restrictions which obstruct widely usage. While in the early years, LF imaging systems were supposed to have a multi-camera array, with organizations such as Lytro and Raytrix, LF cameras have become available for conventional usage. Even if they developed LF systems, because of sensor resolution restriction, there is a trade-off between spatial and angular resolution, and the spatial resolution is lower than 2D conventional imaging systems (Boominathan, Mitra and Veeraraghavan, 2014).

Many studies aim at solving this trade-off have been proposed. These are mostly super-resolution methods that can be applied to spatial dimensions or angular dimensions or both dimensions. Some of these up-to-date methods originate in applying SISR methods to each SAI. Nonetheless, there are some approaches based on the 4D LF structure. Also, methods can be categorized as TIP based methods and NN based methods. The study of (Mitra and Veeraraghavan, 2012) considers modelling LF patches by using Gaussian Mixture Model (GMM), (Rossi and Frossard, 2018) grounds on adoption of multi-frame SR approach, (Farrugia, Galea and Guillemot,

2017) proposes an example-based SR algorithm that learns linear projections between low- and high-resolution dimension and (Alain and Smolic, 2018a) combines an iterative SISR method and LF image denoising. The forementioned works are well-known methods that can be classified as TIP based methods. Along with these studies, some state-of-the-art NN based studies are found, such as the study of (Yoon et al., 2015) grounds on data-driven learning method to upsample the angular and spatial resolution simultaneously, (Yoon et al., 2017) considers applying CNN to simultaneously upsample the spatial and angular resolution respectively, (Wang et al., 2018) proposes a reconstruction scheme based on accumulation of the contextual information from multiple scales.

In this thesis, the LF SR problem is focused since it is an important problem to be solved in the LF imaging technique. By means of traditional and sparsity based approaches, the statistical and visual performance of the developed methods are analyzed. The common point of all developed methods is the usage of LF images around the SAI whose resolution is desired to be upscaled, called LF window. In other words, in these patch-based approaches, it is aimed to increase the similarity by searching the target image patches in the target SAI in the LF window. To find similar image patches, K-nearest neighbors are determined through sum-of-squared distance. Only the nearest patch pairs are calculated for approximation, thus saving computation time and power. Later, LLE known as a dimension reduction method (Roweis and Saul, 2000) and OMP which is a greedy algorithm based on sparse approximations (Pati, Rezaiifar and Krishnaprasad, 1993; Davis, Mallat and Avellaneda, 1997) are used to represent a target reference patch with its K-neighbors. In addition, a local optimization process is applied for ensuring local compatibility. As another common point of proposed methods, IBP or BP is applied for adding details with respect to LR image. All methods presented in this thesis include LF window, LLE or OMP and IBP or BP can provide a new perspective for solving the LF SR problem.

This thesis is organized as follows. The related studies in literature are analyzed briefly in CHAPTER 2: LITERATURE REVIEW. The methods developed in this study are detailed in CHAPTER 3: METHODOLOGY. Statistical and visual results are presented in CHAPTER 4: EXPERIMENTAL DETAILS & RESULTS. Finally, a

brief conclusion and possible future directions are given in CHAPTER 5: CONCLUSION.

CHAPTER 2: LITERATURE REVIEW

2.1 Light Field Denoising, Light Field Superresolution and Stereo Camera Based Refocussing using a GMM Light Field Patch Prior

In the study of (Mitra and Veeraraghavan, 2012), it is proposed a common framework by using a GMM prior for LF patches, such as denoising, angular and spatial SR. The base of this approach is the estimation of LF patches using LMMSE (Kay, 1993) through the estimation of disparity values of extracted patches from the observed data via a fast subspace projection algorithm.

In this method, patches are firstly extracted from the observed image. After that, by analyzing the LF patches of diffuse scenes, LF patches with the same disparity value are showed to lie on a low-dimensional subspace. The LF patches are then modeled as Gaussian random variables depending on their disparity values. In this way, it enables a GMM. In the first step of the processing part to estimate the original LF patches, the disparity value of the observed LF patches is estimated by using a fast subspace projection algorithm PCA (Bartholomew, 2010), as the second part, for each patch, the LMMSE algorithm (Kay, 1993) is used with the estimated disparity value.

In short, being effective and multitasking framework for different LF imaging problems, this method can be considered as a well-known LF SR method.

2.2 Light Field Super-resolution via Graph-based Regularization

In (Rossi and Frossard, 2018), an SR algorithm based on multi-frame approach with graph-based regularizer, called GB, is proposed to provide a global solution to upscale all LF images together. By using this approach, graph-based regularizer that carries out LF structure via nonlocal self-similarities provides to circumvent disparity estimation which can be accepted as a challenging step.

In this study, by designing an iteratively solved quadratic objective function that contain three terms to find the relations between the LF SAIs, LF spatial SR problem can be arranged into a global optimization problem. These three terms consist of the data fidelity compelled to be coherent of HR view and its LR equivalent, warping term that collects the complementary information encoded in each view, graph-based

regularizer that enforces smoothness along the LF epipolar lines defined on the LF structure.

In brief, the method that is generally called Graph-Based Algorithm shows a benchmark performance on LF camera views due to their small disparity values. Thus, this method is one of the significant methods that are used to analyze performance on LF SR.

2.3 Super Resolution of Light Field Images Using Linear Subspace Projection of Patch-Volumes

In (Farrugia, Galea and Guillemot, 2017), to improve the spatial resolution of the different LF views appropriately all SAIs of the LF structure, an example-based SR algorithm is proposed. This algorithm is basically based on learning linear projections between dimension reduced subspaces, in which patch-volumes are extracted from the LF structure.

In the method, example dictionaries are firstly constructed by extracting HR and LR patch pairs from HR and LR LF images. Because they comprise redundant information, and lie on subspaces of lower dimension, the HR and LR patch-volume pairs are projected by using PCA (Bartholomew, 2010). Between the subspaces of HR and LR patch-volumes, a linear mapping function is learned by using RR. With this learned mapping function, LR LF patch-volumes can be upscaled. Also, to prevent disparity of LF structure, a block-matching step is proposed aiming at obtaining best-matching patches across all SAIs. Therefore, the algorithm is named as BM + PCA + RR. In Figure 2, a schematic diagram of the algorithm is illustrated.
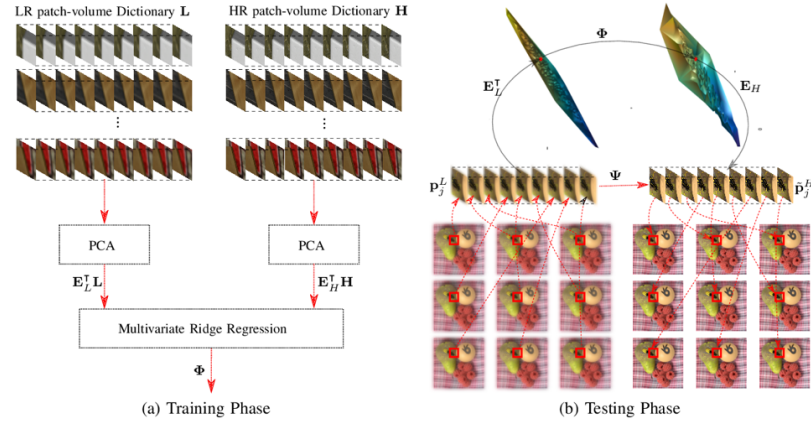
Figure 2. Overview of BM + PCA + RR, (a) the linear projections are learned from training patch-volumes. (b) restoration the LF by using learned projections. (Source: Farrugia, Galea and Guillemot, 2017)

As a result, the proposed approach does not require more training samples, the method can be accepted as a preferred method. However, it is obvious that the method is the one of the old studies in the LF SR literature and does not perform well under different experimental conditions.

2.4 Light Field Super-resolution via LFBM5D Sparse Coding

(Alain and Smolic, 2018a) proposed a spatial SR method combined with the SR-BM3D SISR filter (Egiazarian and Katvonik, 2015) and the LFBM5D LF denoising filter (Alain and Smolic, 2017). The method iteratively updates LF SAIs between LFBM5D filter and BP steps.

In this algorithm, 4D patches consisted by taking 2D patches in the neighboring SAIs with respect to the reference 2D patch. These 4D patches are stacked are stacked to build 5D patches. Then, the 5D LF patches are transformed 5D transform domain due to its high sparsity. Thus, by applying hard-thresholding, sharper HR patches can be estimated using the 5D patches. In the next step, BP is applied on each SAI to add upsampled residual error between the known LF image and downsampled estimated HR image. This process iterates until convergence. Also, image guided filtering is proposed to avoid ringing artifact for high upsampling factors.

In summary, this method presents high performance on low upsampling factors and LF structures that have high disparity value and differ from capturing by LF cameras.

With its sparsity approach and its performance on high disparity value, the method can be considered as a memorable and inspiring LFSR method.

2.5 Learning a Deep Convolutional Network for Light-Field Image Super-resolution

(Yoon et al., 2015) proposes, as accepted one of the earliest NN based LF SR methods a data-driven learning method which is able to upsample angular and spatial dimensions simultaneously. Respectively, the spatial resolution is firstly upsampled by a spatial SR network, then each enhanced view is angularly upscaled using an angular SR network.

In details of the study, the spatial and angular SR networks are trained independently, and then fine-tuned via end-to-end training. As shown in Figure 3, to recover high-frequency details, the networks are fed horizontally, vertically and surrounding bicubic upsampled blocks of each SAI. Also, the reason of the order of this cascade NN structure is that the estimated HR images contain more details and have clean views. The method is called as LFCNN.
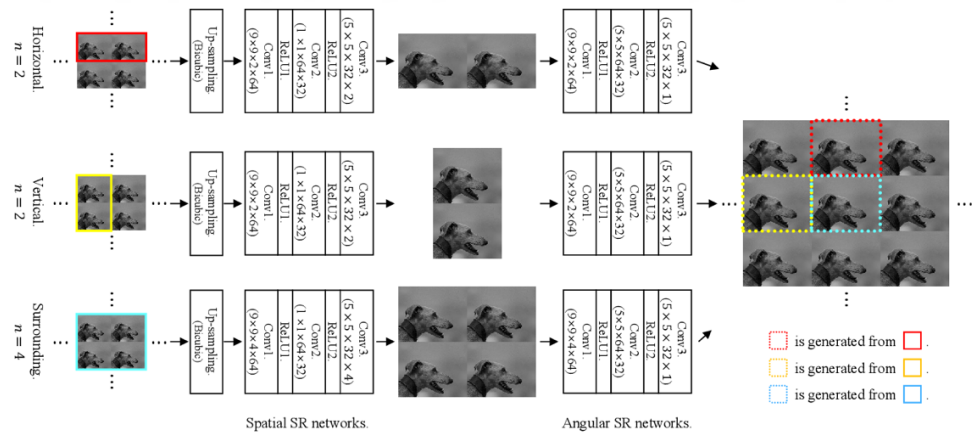
Figure 3. Overview of the LFCNN method. (Source: Yoon et al., 2015)

In brief, this NN based method can be used to obtain estimated HR images by upsampling angular and spatial resolutions simultaneously. However, the given benchmark performance on synthetic LF images may not maintain on LF examples contained high disparity.

2.6 Light Field Image Super-Resolution using Convolutional Neural Network

In (Yoon et al., 2017), the proposed method consists of an improvement of previous cascade NN based LF SR method in "2.5 Learning a Deep Convolutional Network for Light-Field Image Super-resolution" (Yoon et al., 2015). Fundamentally, the method is similar to the previous method that includes spatial and angular SR networks.

Different than the previous study, in this method, the output of the spatial SR network is organized as vertical, horizontal and central pairs to feed angular SR network as shown in Figure 4.
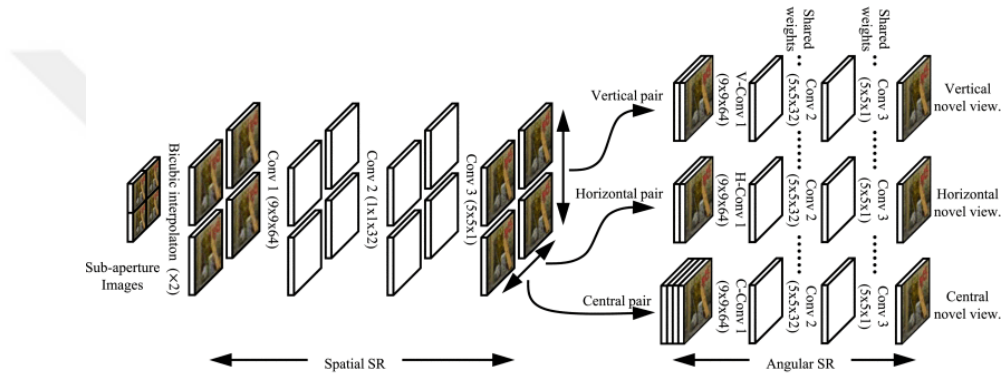
Figure 4. Overview of the improved version of LFCNN. (Source: Yoon et al., 2017)

In short, the proposed method in (Yoon et al., 2017) is a novel version of the study in (Yoon et al., 2015), by changing algorithm pipeline. Also, the given results obtained from LF images, captured in real-world, can enable to evaluate the performance on different LF datasets. Especially, it is also stated that the results in the depth map estimation have been improved.

2.7 LFNet: A Novel Bidirectional Recurrent Convolutional Neural Network for Light-field Image Super-resolution

In the study of (Wang et al., 2018), an NN based method is proposed which uses IMsF scheme to accumulate contextual information from multiscale and Bidirectional Recurrent CNN that iteratively models spatial relations between horizontal and vertical SAIs. This method is named as LFNet.

As shown in Figure 5, LFNet has two NN models specified on directions which are vertical and horizontal to upsample the resolution of vertical and horizontal LF SAIs stacks separately. After that, for obtaining upsampled LF structure, these Bidirectional Recurrent CNN that is used with IMsF are ensembled via stacked generalization.
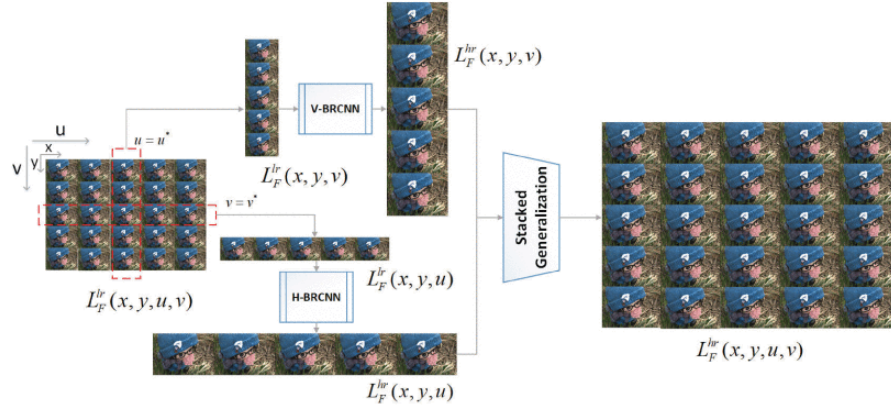
Figure 5. Overview of the LFNet. (Source: Wang et al., 2018)

As a result, LFNet is a NN based method that aims at upsampling LF views as vertical and horizontal stacks. In the light of the presented quantitative and qualitative evaluations on real-world and synthetic datasets, the performance is robust and competitive.

CHAPTER 3: METHODOLOGY

In this chapter, there are different approaches proposed aiming at obtaining an HR LF image which is consistent with neighboring LR LF images. Formally, X_L is the known LR LF and assumed to be a blurred and down-scaled version of the unknown HR LF X_H that is aimed to generate the model as follows:

$$X_L = H_s(X_H) \tag{1}$$

where H_s is the operator of blurring and downsampling of each view with a factor of s.

The described LFSR problem is ill-posed due to the multipotential HR LF X_H generations which can produce exactly the known X_L. To solve the problem, as mentioned in (Türkan, Thoreau and Guillotel, 2013), a global energy function including a prior on X_H is employed:

$$arg \min_{X_H} \|X_L - H_s(X_H)\|_2^2 + \varrho R(X_H) \tag{2}$$

where $\|X_L - H_s(X_H)\|_2^2$ is the data term related to Eq. (2), ϱ and $R(X_H)$ express the control parameter providing contribution of the prior and the regularization term of a prior on X_H, respectively.

In all proposed methodologies in this study, the focus is on solving the LF SR optimization problem in Eq. (2). Firstly, initial estimate $X_{H,0}$ of the HR LF image is obtained by using patch-based estimator:

$$X_{H,0} = arg \min_{X_H} R(X_H) \tag{3}$$

Secondly, to accomplish an image generation model, the data term should be minimized by projecting $X_{H,0}$ onto the solution space of Eq. (1):

$$arg \min_{X_H} \|X_H - X_{H,0}\|_2^2 \quad s.t. \; H_s(X_H) = X_L \tag{4}$$

In the light of this fundamental problem, the proposed solutions are examined in detail in the remaining part of this chapter.

3.1 Common Components of all Proposed Methods

3.1.1 LF Window

As mentioned in the previous section, LF imaging is based on its 4D structure that includes spatial and angular resolutions. Similar to many studies explained in "CHAPTER 2: LITERATURE REVIEW", to upsample each SAI of LF structure, a multi-frame approach that contains neighbors of each SAI is proposed and is called *LF Window* in this thesis. It is aimed to take advantage of this structure in order to use the details of each view on spatial and angular locations. Thus, the focused approximated patch has higher precision by using the similarities of adjacent textures in different views in LF structure. For each SAI, neighboring SAIs in the LF Window are considered from the LF structure as shown in Figure 6.
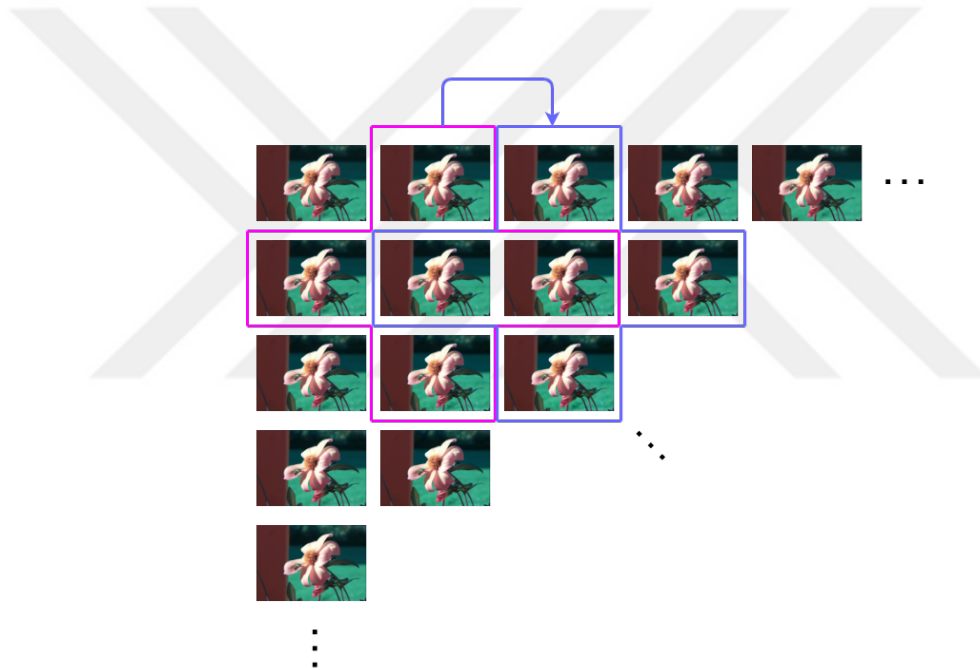
Figure 6. An example of LF Window sliding on 4D LF Structure.

3.1.2 Phase Images

As detailed in (Glasner, Bagon and Irani, 2009), small image patches generally repeat themselves within and across different scales of an image. Therefore, as shown in Figure 7, exemplar LR and HR patch pairs from each LR LF SAI are collected respectively from its downscaled version of LR LF patches located in the downscaled LR LF SAIs and their related HR LF parents according to input LR LF SAI.
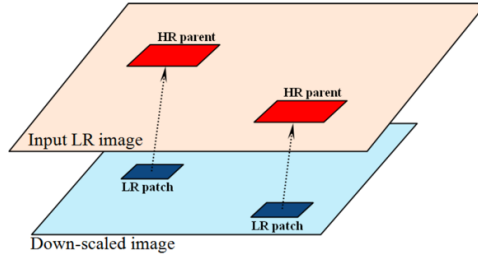
Figure 7. Collection LR and HR patch pairs from the input LR LF SAI and its downscaled version. (Source: Türkan, Thoreau and Guillotel, 2013)

According to (Freedman and Fattal, 2011), to conserve various details of natural images, using small scaling factors is a principle of improving the resolution. Hence, in this thesis, all proposed methods use small scaling ratios to reach satisfied upsampling factors at each step, as used in (Türkan, Thoreau and Guillotel, 2013). Also, with this small scaling ratios, at each step, LR LF and HR LF patch pairs are extracted from each LF SAI in the *LF Window*. For increment the size of LR LF patch of size $n \times n$, tp-pixels are added at each step $0 < t < \tau$, thus by using $l_{i,sai}^{t-1}$ of size $(n \times (t-1)p) \times (n \times (t-1)p)$, $l_{i,sai}^{t}$ of size $(n \times tp) \times (n \times tp)$ can be obtained. A HR LF patch pair $h_{i,sai}^{t}$ of sizes $(n \times tp) \times (n \times tp)$ is also extracted from input LR LF SAI and its matching LR LF exemplar of size $(n \times (t-1)p) \times (n \times (t-1)p)$ in $s_t = (n \times (t-1)p)/(n + tp)$ times downscaled LR LF SAI. In order to provide that LR and HR patch pairs are in *phase*, with using non-integer s_t, irregular points of input LR and its downscaled version images have to be related. To search and match patch pair regular offset, at step t, multiple downscaled *phase image* $\Phi_{q,sai}^{t}$ are created by offsetting each input LR LF SAI by $0 \ldots n + (t-1)p - 1$ pixels in each spatial dimension. Basically, that means q is equal to $0 \ldots (n + tp) \times (n + tp) - 1$. With respect to *phase images* for each SAI, LR LF and HR LF patch pairs are obtained.

3.1.3 Nearest Neighbor Search

After obtaining LR LF and HR LF patch pairs as previously explained, a nearest neighbor search is proposed to eliminate highly redundant LF patches far from reference LF patch. Thus, to save computational power and time, the neighbor approximation methods are applied only on the patch pairs closest to reference LF

patch. For each focused reference patch in center SAI in the *LF Window*, at each step t, K-NN patches are found and stacked to be used on the HR patch estimation. In each phase image, the determined K number is equal to the number of neighbors in the LLE optimization and the number of iterations in OMP. Especially, for OMP, the rank of the collected stack is checked on each step to satisfy over-completeness.

3.1.4 Local Optimization

As detailed in (Türkan, Thoreau and Guillotel, 2013), at any step t, the estimated HR LF patch is downscaled to match patch size with reference input LR LF patch. The L_2 distance between downscaled estimated HR LF patch and reference LR LF patch is calculated to check the similarity between them. To verify the local patch compatibility, the best estimation of HR LF patch is selected to be used in the HR reconstruction. This optimization step is applied on LLE and OMP differently. In the LLE based approach, it is applied to the results from different number of neighbors from 1 to K, while it is applied to the results from each iteration (from 1 to K) in OMP.

3.1.5 Back-Projection

To ensure the consistency between the reconstructed HR LF center SAI in the *LF Window* and the input LR LF center SAI in the *LF Window*, BP or IBP is proposed as a final step of all proposed methods. To solve Eq. (4), BP is formulated as follows:

$$X_{H,center} = X_{H,center,0} + \beta\left[\left(X_{L,center} - \left(X_{H,center,0} * B\right) \downarrow_s\right) \uparrow_s\right] * P \quad (5)$$

where $X_{H,center}$ is the final estimated HR LF center SAI , $X_{H,center,0}$ is the inital estimation of HR LF center SAI, $X_{L,center}$ is the input LR LF center SAI, B and P are blur kernel and back-projection kernel, and $*$, $\uparrow_s$, $\downarrow_s$ represent 2D convolution, up- and down-scaling operators with a factor of s, respectively. Also, as used in (Egiazarian and Katvonik, 2015; Alain and Smolic, 2018a), β provides a weight for the residual error.

BP process can also be applied iteratively. This can be seen as an approach where consistency is ensured and various features are added in each iteration. Similar to Eq. (5), IBP can be formulated as follows:

$$X_{H,center,m} = X_{H,center,m-1} + \beta\left[\left(X_{L,center} - \left(X_{H,center,m-1} * B\right) \downarrow_s\right) \uparrow_s\right] * P \quad (6)$$

where $X_{H,center,m}$ is the estimated HR LF center SAI at iteration $m, m = 1 \ldots M,$ and the remaining terms and operations are the same as BP.

The difference between BP and IBP is that BP is non-iterative, it does not smooth LF images at every iteration as IBP does. This effect may also be observed with the experimental results in "CHAPTER 4: EXPERIMENTAL DETAILS & RESULTS".

3.2 Neighbor Approximation Methods

3.2.1 Locally Linear Embedding

The proposed technique is inspired from the well-known dimensionality reduction approach called LLE (Roweis and Saul, 2000). The adapted algorithm focuses on approximating HR LF patches through neighboring LR LF patches taken from exemplar patch pairs. Thus, neighbor embedding optimization is given as follows:

$$arg \min_{X_H} \left\| l_{i,center}^{t-1} - \sum_k w_{i,k} l_{i,sai}^t \right\|_2^2 \quad subject\ to \sum_k w_{i,k} = 1 \qquad (7)$$

where $w_{i,k}$ represents the approximation weights stated for the K-NN, $l_{i,sai}^t$. Additionally, weighting coefficients are constrained by a sum-to-one constraint to provide shift-invariance. This constrained optimization is solved in a similar way as in (Roweis and Saul, 2000). Finally, HR LF patches are estimated at each step t by multiplying the optimum weights with $h_{i,sai}^t$.

3.2.2 Orthogonal Matching Pursuit

OMP is a sparsity based greedy approach to solve ill-posed problems. As seen in the detailed study of (Yang et al., 2010), sparsity notion can be applicable to robustly solve SR optimization problems. By adopting this perspective, the proposed method uses K-NN constrained LR LF patches as a dictionary for OMP in order to reconstruct HR LF center SAI in the *LF Window*. Thus, at each iteration, the sparse vector is updated using the LR LF dictionary. With the calculated sparse vector, HR LF patches are estimated in center SAI in the *LF Window*. Additionally, an adapted OMP called *MeanSubs-OMP*, is employed over the mean subtracted values of each dictionary element (i.e., atom). The aim here is to highlight the texture in the patches with this mean subtraction. After the estimation of HR LF patches in center SAI, the corresponding mean value of HR LF patches is added to the final estimation.

3.3 Proposed Methods in this Study

In this part, detailed overviews of the proposed methods are described. The approaches explained in the previous subsections are combined in the proposed methods. The general idea of the proposed algorithms basically originates from (Türkan, Thoreau and Guillotel, 2013). Because, as detailed before, it is observed that the different texture information in the angular and spatial dimensions of the LF structure has an important role in upscaling the resolution. Hence, it is proposed that the exemplar-based approach can provide significant advantages in the LF structure, especially by searching for texture similarity in different phase images.

3.3.1 Optimized Locally Linear Embedding Based Nearest Neighbor Constraint Light Field Super-Resolution (OptLLE-LFSR)

This proposed algorithm is mainly based on LLE with *Local Optimization* and named as *OptLLE-LFSR*. As previously detailed, the *LF Window* is first created to focus on specific LF SAIs for each SAI to be upsampled. The phase images of each SAI are produced and, LR LF and HR LF patch pairs are then extracted. As illustrated in Figure 8, at each step t, to upscale LR LF patches with non-integer ratios, HR LF patches are firstly estimated by using LLE with local optimization. Basically, the output patch stack at a specific step is the reference patch stack for the following step. Finally, the proposed method is completed by applying IBP after the reconstruction of overlapping patches by s pixels in both directions.

3.3.2 Optimized Orthogonal Matching Pursuit Algorithm Based Nearest Neighbor Constraint Light Field Super-Resolution via Deblurring with Self-Organizing Map (OptOMP-LFSR via SOM)

The designed algorithm in this part contains OMP with *Local Optimization* to solve LF SR optimization problem with sparse representations, and it is named as *OptOMP-LFSR via SOM*. As shown in Figure 9, the flow of the algorithm is indeed similar to the previously proposed method. However, *SOM* and BP with image guided filter (He, Sun and Tang, 2013) are applied to resolve blur artifacts on the reconstructed LF views. SOM is employed to enhance the details by means of the principle of the study in (Kohonen, 1990) . For each $d \times d$ block in the image, the mean value is subtracted

from the block. This mean subtracted block is then multiplied by ς and added to initial $d \times d$ block. In this way, the local content of the image is recovered. It is also observed during different trials that IBP has negative effects of smoothing. Thus, BP is preferred in the following methods.

3.3.3 Optimized Orthogonal Matching Pursuit Algorithm Based Nearest Neighbor Constraint Light Field Super-Resolution via Edge Directed Unsharp Masking Sharpening Method (OptOMP-LFSR via EDUMS)

The flowchart of the developed method in this part is shown in Figure 10. It is named as *OptOMP-LFSR via EDUMS*, because of the employed techniques: *Local Optimization* and *Edge Directed Unsharp Masking Sharpening* (Peng et al., 2013). In the *EDUMS*, the normalized component edge information from Canny Edge (Canny, 1986) is employed to suppress the edge jaggies. Even though *EDUMS* is proposed for real-time video applications, performance improvements are observed in the proposed approach (See in "CHAPTER 4: EXPERIMENTAL DETAILS & RESULTS").

3.3.4 Optimized Mean Substracted Orthogonal Matching Pursuit Algorithm Based Nearest Neighbor Constraint Light Field Super-Resolution via Deblurring with Self-Organizing Map (OptMeanSubs-OMP-LFSR via SOM)

This proposed method differs from the previous method called *OptOMP-LFSR via SOM,* by including *MeanSubs-OMP* and applying *SOM* to $X_{L,center}$ without the *P* kernel in *BP*. Thus, it is called as *OptMeanSubs-OMP-LFSR via SOM*. In particular, the application of *SOM* to $X_{L,center}$ in *BP* helps emphasize details by reducing the approximation of input blur image. The flowchart of the algorithm is illustrated in Figure 11.
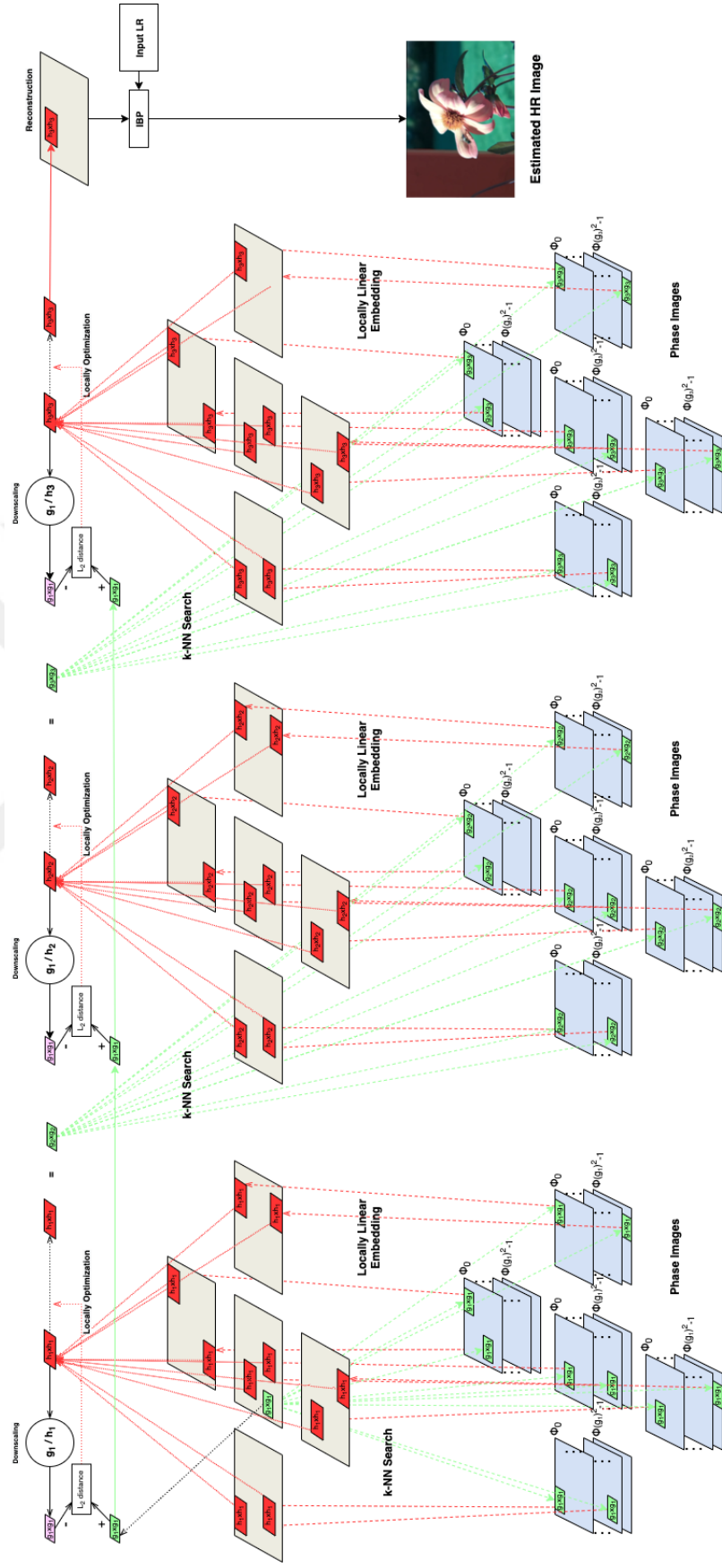
Figure 8. Schematic Diagram of OptLLE-LFSR
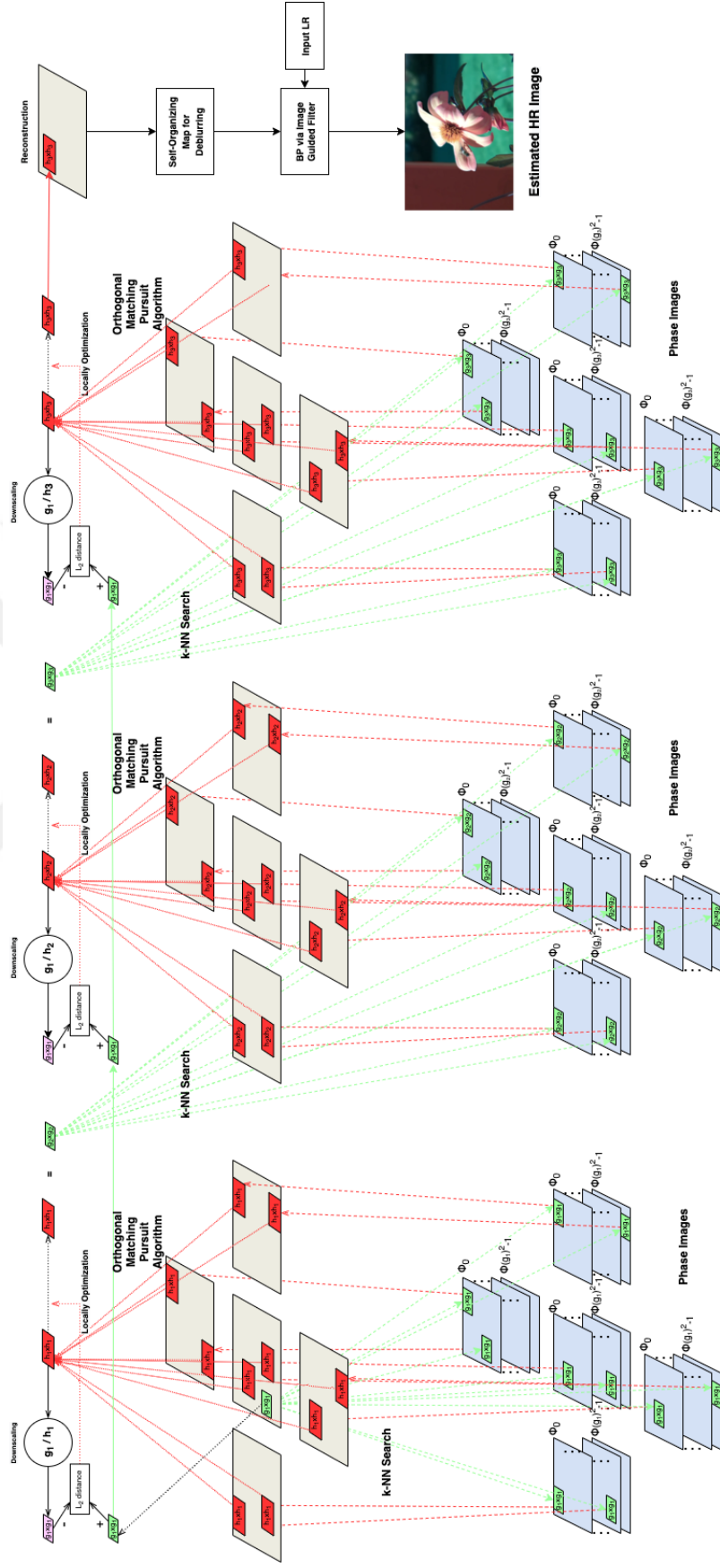
Figure 9. Framework of OptOMP-LFSR via SOM

19
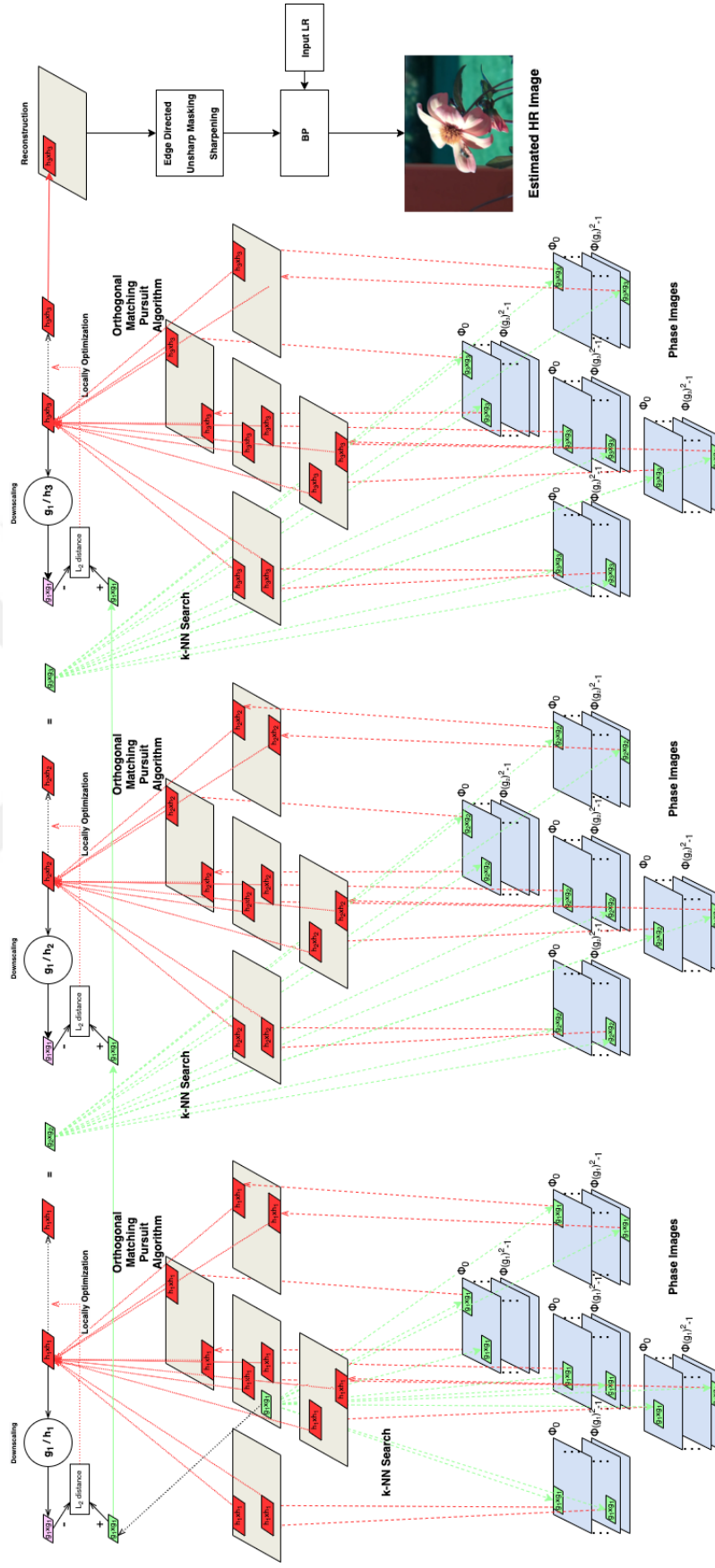
Figure 10. An Illustration of OptOMP-LFSR via EDUMS
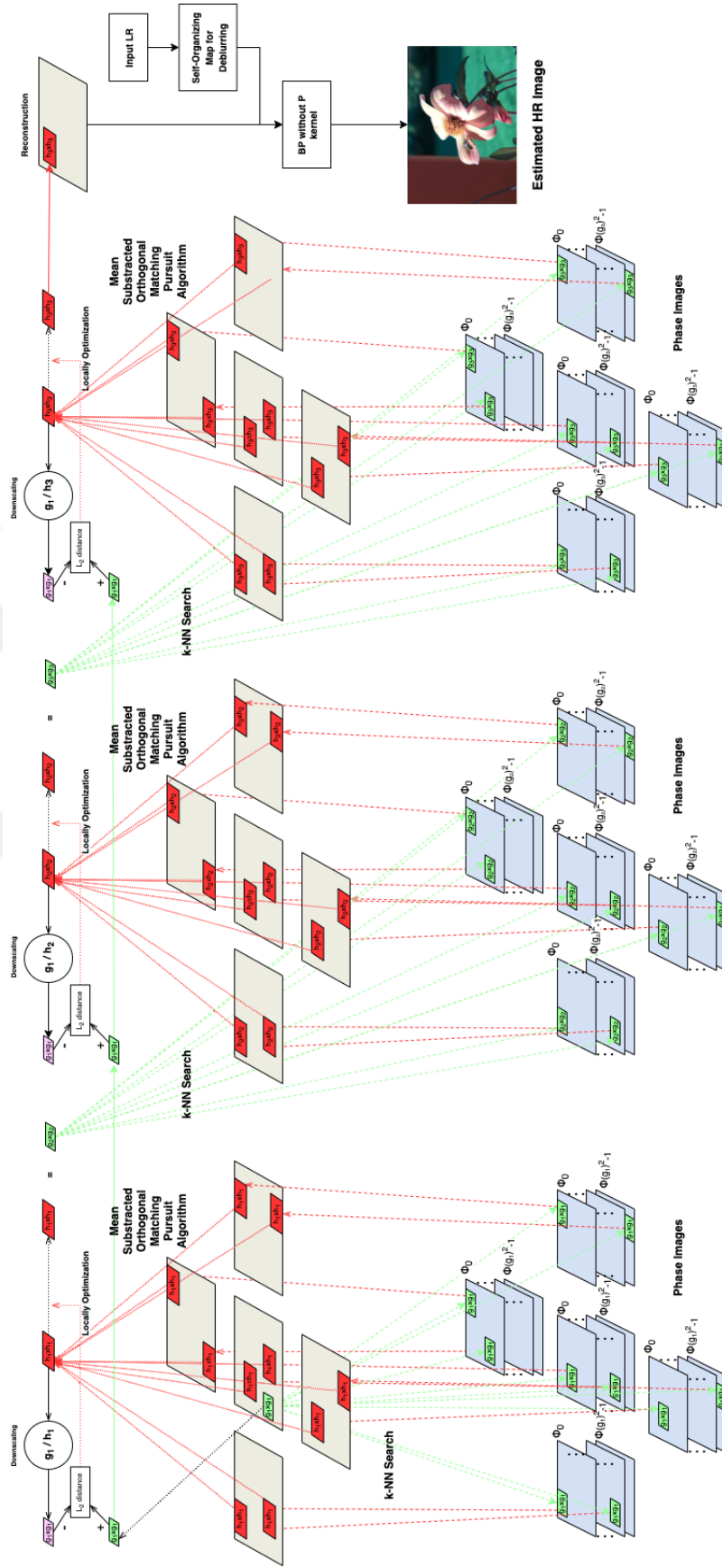
Figure 11. Schematic Diagram of OptMeanSubs-OMP-LFSR via SOM.

CHAPTER 4: EXPERIMENTAL DETAILS & RESULTS

In this chapter, experimental results of each proposed method are presented visually and statistically to examine the performance of these algorithms. Besides, statistical results of miscellaneous well-known benchmark SISR and LF SR methods are discussed for comparison, for instance, Bicubic interpolation, SR-BM3D (Egiazarian and Katvonik, 2015), BM + PCA + RR (Farrugia, Galea and Guillemot, 2017), GB (Rossi and Frossard, 2018), and SR-LFBM5D (Alain and Smolic, 2018a). The statistical results were taken from the project website (Alain and Smolic, 2018b) of the study (Alain and Smolic, 2018a) and extended on its basis.

All implementations have been carried out on MATLAB R2022a environment. All test images are shown in Figure 12. Lytro Illum dataset is processed as in (Matysiak et al., 2020), used as the experimental dataset. It consists of EPFL LF Image Dataset (Rerabek and Ebrahimi, 2016) and Inria Lytro Illum LF Dataset (Le Pendu, Jiang and Guillemot, 2018). This dataset is an extensively used one in LF image processing studies.
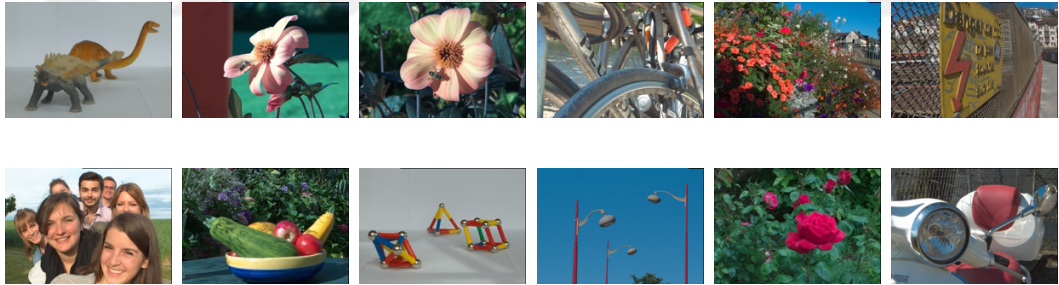
Figure 12. Lytro Illum Dataset

4.1 Experimental Details

The centering 5×5 SAIs in the LF structure is used for computation time. The scaling factor s is set to 2 and 3. To generate LF images, downscaling operator and Gaussian blurring kernel are applied on each SAI, and Gaussian blurring kernel is set with standard deviation 1.6 and of sizes $7 \times 7, 9 \times 9$ for $s = 2 \ and \ 3$, respectively. In the experiments, LR patch size is set to $n = 3$, thus for $\tau = 3$, $\{s_1, s_2, s_3\}_{s=2} = \{3/4, 4/5, 5/6\}$ and $\{s_1, s_2, s_3\}_{s=3} = \{3/5, 5/7, 7/9\}$. To compute the PSNR score,

in order not to be affected by the edge artifacts, the reconstructed HR image is cropped by 20 pixels from rows and columns in the borders.

4.1.1 Experimental details of OptLLE-LFSR

In this experiment, all SAIs in the *LF* Window are applied with imsharpen filter to eliminate blur, i.e. where standard deviation of Gaussian low-pass filter is set to 1 and Strength of sharpening effect is set to 0.8. For Nearest Neighbor Search and LLE, $K = 8$. For IBP, $M = 10$ when $s = 2$, $M = 30$ when $s = 3$ with, and $\beta = 1.85$ and $\uparrow_s$, $\downarrow_s$ are set to bicubic upsampling and downsampling filters.

4.1.2 Experimental details of OptOMP-LFSR via SOM

In this experiment, for Nearest Neighbor Search and OMP, K and number of iterations is set to 10. Also, in OMP, stopping threshold value for approximation error is set to 0.001. For BP, $\beta = 2.85$ and $\uparrow_s$, $\downarrow_s$ are set to bicubic upsampling and downsampling. For SOM, $d = 2$ and $\varsigma = 0.04$.

4.1.3 Experimental details of OptOMP-LFSR via EDUMS

In this experiment, for Nearest Neighbor Search and OMP, K and the number of iterations is same as previously defined. In OMP, threshold error value is set to 0.001. For BP, $\beta = 2.25$ and $\uparrow_s$, $\downarrow_s$ are set bicubic upsampling and downsampling.

4.1.4 Experimental details of OptMeanSubs-OMP-LFSR via SOM

Similar to previous experiments, for Nearest Neighbor Search and *MeanSubs-OMP*, K and the number of iterations is defined as 10. Threshold value is set to 0.001. In BP, $\beta = 1.55$ and $\uparrow_s$, $\downarrow_s$ are set bicubic upsampling and downsampling. To apply SOM on $X_{L,center}$, $d = 2$ and $\varsigma = 0.4$.

4.2 Experimental Results

In this section, statistical and visual results of the proposed methods and benchmark methods are presented. The proposed methods are compared against Bicubic Interpolation, SR-BM3D (Egiazarian and Katvonik, 2015), BM + PCA + RR (Farrugia, Galea and Guillemot, 2017), GB (Rossi and Frossard, 2018) and SR-LFBM5D (Alain and Smolic, 2018a). The statistical results in terms of PSNR (in dB)

are reported in Table 1, Table 2, and Table 3. For each LF view, the scores of the focused 5×5 centering SAIs in the LF structure are computed as average PSNR (in dB) values.

The experimental results reported in Table 1 show that the proposed algorithms produce competitive results among all average PSNR scores for $s = 2 \ and \ 3$. According to average results of *OptMeanSubs-OMP-LFSR via SOM*, this method outperforms most of the benchmark studies. For $s = 2$, the average results of *OptOMP-LFSR via SOM* and *OptOMP-LFSR via EDUMS* are higher than those of the benchmark algorithms. Furthermore, for $s = 2$, it is observed that SOM has a better improvement than EDUMS. In the average results of $s = 3$, *OptOMP-LFSR via EDUMS* and *OptMeanSubs-OMP-LFSR via SOM* perform close to or better than the benchmark studies. Unlike for $s = 2$, EDUMS presents higher experimental scores than SOM for $s = 3$. According to the average performance statistics, OMP provides better results than LLE regardless of the value of s. Especially for $s = 2$, the methods based OMP have highly competitive statistical results. With all these evaluations and average performance scores in Table 1, it is clearly noticed that *MeanSubs-OMP* approach is the much better performing one.

Table 1. Average performances in PSNR (dB)

Methods	$s = 2$	$s = 3$
Bicubic	27.78	26.08
SR-BM3D (Egiazarian and Katvonik, 2015)	30.21	28.45
BM + PCA + RR (Farrugia, Galea and Guillemot, 2017)	29.95	28.55
GB (Rossi and Frossard, 2018)	29.80	28.65
SR-LFBM5D 1st Step (Alain and Smolic, 2018)	30.17	28.62
SR-LFBM5D 2nd Step (Alain and Smolic, 2018)	30.25	28.60
OptLLE-LFSR	30.08	27.48
OptOMP-LFSR via SOM	30.95	28.12
OptOMP-LFSR via EDUMS	30.57	28.64
OptMeanSubs-OMP-LFSR via SOM	**31.30**	**28.90**

The detailed statistical results in Table 2 report the image quality scores for $s = 2$. *OptMeanSubs-OMP-LFSR via SOM* method provides the highest PSNR value on *Ankylosorus*, *Bee1*, *Bee2*, *Fruits*, *Posts*, *Rose* and *Vespa* LF datasets. Moreover, all proposed methods outperform on these datasets except *Ankylosorus*, *Fruits* and *Vespa* datasets. It is also worth mentioning that the proposed main approach, which is exemplar-based and non-integer ratio upsampling in multi-times, is successful at a low upsampling factors for $s = 2$.

The results reported in Table 3 show the PSNR scores for $s = 3$. In *Bee1*, *Bee2*, *Posts* and *Rose* LF dataset, *OptMeanSubs-OMP-LFSR via SOM* has the best performance against all benchmark algorithms. It is also observed that all proposed methods show the highest performance on *Posts* LF dataset for $s = 3$ as for $s = 2$.

In the light of these statistical results and the visual results are shown from Figure 13 to Figure 24 for $s = 2$, the outcomes of *OptMeanSubs-OMP-LFSR via SOM* have more details and less blurring artifacts visually. The results of LF views that have more detail, such as *Chez Edgar* (in Figure 17), *Danger de Mort* (in Figure 18) and *Friends 1* (in Figure 19), have not enough improvements for blur. In addition, the results of *Ankylosorus* (in Figure 13), *Bee 1* (in Figure 14), *Bee2* (in Figure 15), *Fruits* (in Figure 20), *Posts* (in Figure 22), *Rose* (in Figure 23) and *Vespa* (in Figure 24) contain fine-detailed textures, such as, flower petal in *Bee 1* (in Figure 14), *Bee2* (in Figure 15), *Rose* (in Figure 23), post's chandelier or column in *Posts* (in Figure 22) and headlight in *Vespa* (in Figure 24). As it can be supported by statistical results, *OptLLE-LFSR* is not applicable to remove the blur or recover fine-details. Even though *OptOMP-LFSR via SOM* and *OptOMP-LFSR via EDUMS* can reconstruct sharper images, a certain amount of blur is still present. If a full inference is to be made for $s = 2$, it is observed that the proposed methods achieve plausible results with low disparity in the LF views focused on a particular object.

The visual results of *OptMeanSubs-OMP-LFSR via SOM* for $s = 3$ are shown from Figure 25 to Figure 36. These can be visually evaluated as sharper images. Because of the larger upsampling factor, it is expected that the estimated HR images are more blurred than the $s = 2$ results. Thus, the results of proposed methods are not

satisfactory because the methods perform far from removing the blur and preserving fine-detail. For example, this is observed in Figure 25 (*Ankylosorus*), Figure 32 (*Fruits*), Figure 36 (*Vespa*). Besides, the results of *Bee 1* (in Figure 26), *Bee 2* (in Figure 27), *Posts* (in Figure 34) and *Rose* (in Figure 35) have sharper and detailed views. Especially, the details of petal texture in *Bee 1* (in Figure 26), *Bee 2* (in Figure 27) and post's chandelier or column in *Posts* (in Figure 22) can be easily distinguished. Additionally, *OptMeanSubs-OMP-LFSR via SOM* provides better visual quality with texture details on all LF views. It is mentioned that *OptMeanSubs-OMP-LFSR via SOM* cannot recover as much detail as and eliminate the blur, when compared to $s = 2$.

To sum up, the proposed methods produce visually appealing results of the LF views contained low disparity and texture, such as *Bee 1* (in Figure 14 and Figure 26), *Bee 2* (in Figure 15 and Figure 27), *Posts* (in Figure 22 and Figure 34) and *Rose* (in Figure 23 and Figure 35). On the other hand, the proposed exemplar-based approach cannot provide the desired statistical and visual performance for images with high disparity or texture details (i.e., *Chez Edgar* (in Figure 17 and Figure 29), *Danger de Mort* (in Figure 18 and Figure 30), *Friends 1* (in Figure 19 and Figure 31)).

Table 2. Detailed statistical results in PSNR (dB), s=2

LF Name	Bicubic	SR-BM3D (Egiazarian and Katvonik, 2015)	BM + PCA + RR (Farrugia, Galea and Guillemot, 2017)	GB (Rossi and Frossard, 2018)	SR-LFBM5D 1st Step (Alain and Smolic, 2018)	SR-LFBM5D 2nd Step (Alain and Smolic, 2018)	OptLLE – LFSR	OptOMP-LFSR via SOM	OptOMP-LFSR via EDUMS	OptMeanSubs-OMP-LFSR via SOM
Ankylosorus	33.5414	36.0750	35.6127	35.7291	36.0440	36.1230	35.6605	36.8278	36.1597	**37.1758**
Bee 1	27.0979	29.0230	28.7435	28.7144	28.9920	29.0370	29.6467	30.8348	30.3829	**31.2654**
Bee 2	27.5808	29.3460	29.0858	29.1590	29.3030	29.3500	31.1858	32.6684	31.5493	**32.8243**
Bikes	26.2794	30.0580	29.5911	29.3290	29.9770	30.0980	28.0466	28.9629	28.7347	29.4701
Chez Edgar	22.3877	24.2200	24.2046	23.7530	24.2220	24.2820	23.4787	23.7661	23.7599	24.0551
Danger de Mort	24.3675	27.1010	26.8869	26.6180	27.0590	27.1440	25.9229	26.3446	26.2772	26.8541
Friends 1	28.7130	32.1850	31.8674	31.6290	32.1360	32.2420	30.2719	31.5777	30.9916	31.9224
Fruits	26.0159	28.7910	28.6242	28.2490	28.7140	28.8160	28.3002	29.1635	28.9295	**29.6661**
Magnets 1	31.0621	33.8580	33.4409	33.3530	33.8400	33.8990	32.5851	33.3032	32.9340	33.6340
Posts	30.4165	30.9580	30.8375	30.9148	30.9170	30.9660	34.9897	35.1932	35.0798	**35.1407**
Rose	28.5095	30.5970	30.4213	30.2920	30.4950	30.6020	31.5348	32.3000	31.8875	**32.6190**
Vespa	27.3734	30.3540	30.1102	29.9180	30.3260	30.4250	29.3189	30.4080	30.1812	**30.9524**

27

Table 3. Detailed statistical results in PSNR (dB), s=3

LF Name	Bicubic	SR-BM3D (Egiazarian and Katvonik, 2015)	BM + PCA + RR (Farrugia, Galea and Guillemot, 2017)	GB (Rossi and Frossard, 2018)	SR-LFBM5D 1st Step (Alain and Smolic, 2018)	SR-LFBM5D 2nd Step (Alain and Smolic, 2018)	OptLLE-LFSR	OptOMP-LFSR via SOM	OptOMP-LFSR via EDUMS	OptMeanSubs-OMP-LFSR via SOM
Ankylosorus	31.5025	34.2070	34.3607	**34.6060**	34.5590	34.5320	32.6369	33.6819	34.5280	34.5756
Bee 1	25.4013	27.8920	27.6675	27.7740	27.9210	27.9080	26.8279	27.9763	28.5994	**28.9620**
Bee 2	25.9392	28.2650	28.2250	28.3950	28.3660	28.3480	28.1788	28.7892	30.1712	**30.4034**
Bikes	24.5069	27.9780	27.8739	28.0730	**28.1270**	28.1150	25.6460	27.0065	26.7293	27.1395
Chez Edgar	21.1371	22.4330	**22.7327**	22.6440	22.4590	22.4390	21.8962	22.0747	22.1231	22.3627
Danger de Mort	22.8849	24.9790	25.2586	**25.3560**	25.1710	25.1330	23.7575	24.4295	24.0787	24.4463
Friends 1	26.5890	30.4230	30.4348	**30.5310**	30.5290	30.5130	27.4232	28.9652	29.4298	29.9185
Fruits	24.3747	26.8270	**27.1949**	27.1590	27.1390	27.1060	25.7651	26.2772	26.7923	27.1673
Magnets 1	29.0306	31.5000	31.5474	**31.6720**	31.5860	31.5730	29.9232	30.7302	30.8570	30.9675
Posts	29.2154	29.6670	29.7040	29.7810	29.7670	29.7680	32.2611	31.0606	32.5569	**32.4164**
Rose	26.8529	28.7330	28.9552	28.9760	29.0390	29.0070	28.8094	28.6867	29.6671	**29.9508**
Vespa	25.5526	28.5340	28.0678	**28.7810**	28.7560	28.7310	26.6785	27.7809	28.1215	28.5202

Original

Bicubic

OptLLE-LFSR

OptOMP-LFSR via SOM

OptOMP-LFSR via EDUMS

OptMeanSubs-OMP-LFSR via SOM

Figure 13. Visual results of Ankylosorus, $s = 2$

Original

Bicubic

OptLLE-LFSR

OptOMP-LFSR via SOM

OptOMP-LFSR via EDUMS

OptMeanSubs-OMP-LFSR via SOM

Figure 14. Visual results of Bee1, $s = 2$

Original

Bicubic

OptLLE-LFSR

OptOMP-LFSR via SOM

OptOMP-LFSR via EDUMS

OptMeanSubs-OMP-LFSR via SOM

Figure 15. Visual results of Bee2, $s = 2$

Original

Bicubic

OptLLE-LFSR

OptOMP-LFSR via SOM

OptOMP-LFSR via EDUMS

OptMeanSubs-OMP-LFSR via SOM

Figure 16. Visual results of Bikes, $s = 2$

Original

Bicubic

OptLLE-LFSR

OptOMP-LFSR via SOM

OptOMP-LFSR via EDUMS

OptMeanSubs-OMP-LFSR via SOM

Figure 17. Visual result of Chez Edgar, $s = 2$

Original   Bicubic

OptLLE-LFSR   OptOMP-LFSR via SOM

OptOMP-LFSR via EDUMS   OptMeanSubs-OMP-LFSR via SOM

Figure 18. Visual result of Danger de Mort, $s = 2$

Original

Bicubic

OptLLE-LFSR

OptOMP-LFSR via SOM

OptOMP-LFSR via EDUMS

OptMeanSubs-OMP-LFSR via SOM

Figure 19. Visual results of Friends 1, $s = 2$

Original

Bicubic

OptLLE-LFSR

OptOMP-LFSR via SOM

OptOMP-LFSR via EDUMS

OptMeanSubs-OMP-LFSR via SOM

Figure 20. Visual results of Fruits, $s = 2$

Original

Bicubic

OptLLE-LFSR
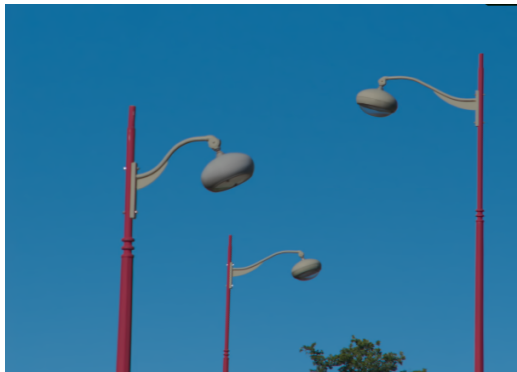
OptOMP-LFSR via SOM

OptOMP-LFSR via EDUMS

OptMeanSubs-OMP-LFSR via SOM

Figure 21. Visual results of Magnets 1, $s = 2$

Original

Bicubic

OptLLE-LFSR

OptOMP-LFSR via SOM

OptOMP-LFSR via EDUMS

OptMeanSubs-OMP-LFSR via SOM

Figure 22. Visual results of Posts, $s = 2$

Original

Bicubic

OptLLE-LFSR

OptOMP-LFSR via SOM

OptOMP-LFSR via EDUMS

OptMeanSubs-OMP-LFSR via SOM

Figure 23. Visual results of Rose, $s = 2$

Original

Bicubic

OptLLE-LFSR

OptOMP-LFSR via SOM

OptOMP-LFSR via EDUMS

OptMeanSubs-OMP-LFSR via SOM

Figure 24. Visual results of Vespa, $s = 2$

Original

Bicubic

OptLLE-LFSR

OptOMP-LFSR via SOM

OptOMP-LFSR via EDUMS

OptMeanSubs-OMP-LFSR via SOM

Figure 25. Visual results of Ankylosorus, $s = 3$

Original

Bicubic

OptLLE-LFSR

OptOMP-LFSR via SOM

OptOMP-LFSR via EDUMS

OptMeanSubs-OMP-LFSR via SOM
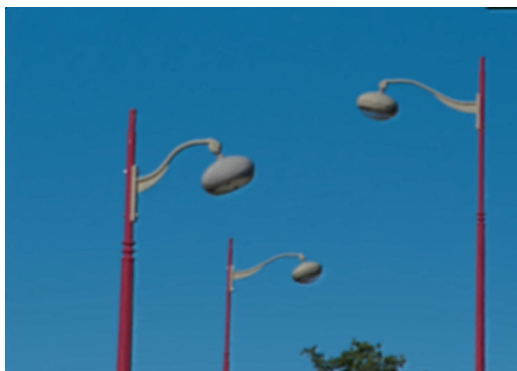
Figure 26. Visual results of Bee 1, $s = 3$

Original

Bicubic

OptLLE-LFSR

OptOMP-LFSR via SOM

OptOMP-LFSR via EDUMS

OptMeanSubs-OMP-LFSR via SOM

Figure 27. Visual results of Bee2, $s = 3$

Original

Bicubic

OptLLE-LFSR

OptOMP-LFSR via SOM

OptOMP-LFSR via EDUMS

OptMeanSubs-OMP-LFSR via SOM

Figure 28. Visual results of Bikes, $s = 3$

Original

Bicubic

OptLLE-LFSR

OptOMP-LFSR via SOM

OptOMP-LFSR via EDUMS

OptMeanSubs-OMP-LFSR via SOM

Figure 29. Visual results of Chez Edgar, $s = 3$

Original

Bicubic

OptLLE-LFSR

OptOMP-LFSR via SOM

OptOMP-LFSR via EDUMS

OptMeanSubs-OMP-LFSR via SOM

Figure 30. Visual results of Danger de Mort, $s = 3$

Original

Bicubic

OptLLE-LFSR

OptOMP-LFSR via SOM

OptOMP-LFSR via EDUMS

OptMeanSubs-OMP-LFSR via SOM

Figure 31. Visual results of Friends 1, $s = 3$

Original

Bicubic

OptLLE-LFSR

OptOMP-LFSR via SOM

OptOMP-LFSR via EDUMS

OptMeanSubs-OMP-LFSR via SOM
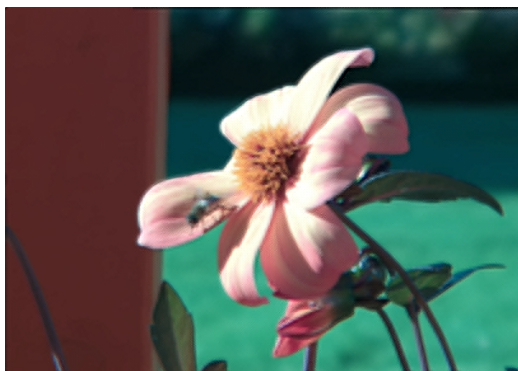
Figure 32. Visual results of Fruits, $s = 3$

Original

Bicubic
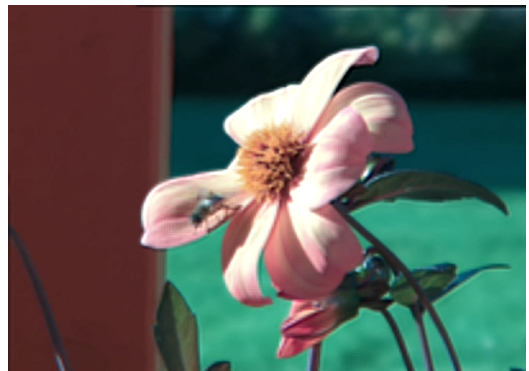

OptLLE-LFSR

OptOMP-LFSR via SOM

OptOMP-LFSR via EDUMS

OptMeanSubs-OMP-LFSR via SOM

Figure 33. Visual results of Magnets 1, $s = 3$

Original

Bicubic

OptLLE-LFSR

OptOMP-LFSR via SOM

OptOMP-LFSR via EDUMS

OptMeanSubs-OMP-LFSR via SOM

Figure 34. Visual results of Posts, $s = 3$

Original

Bicubic

OptLLE-LFSR

OptOMP-LFSR via SOM

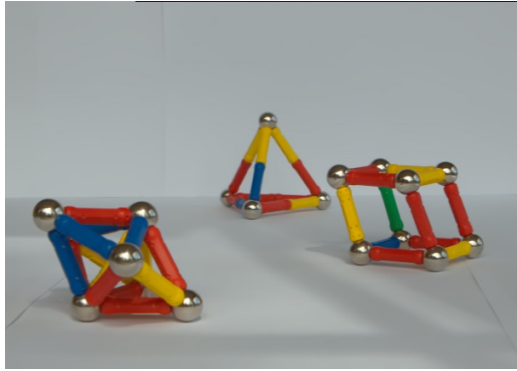OptOMP-LFSR via EDUMS

OptMeanSubs-OMP-LFSR via SOM

Figure 35. Visual results of Rose, $s = 3$
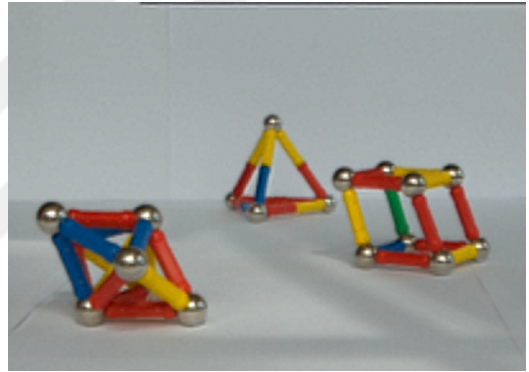
Original   Bicubic

OptLLE-LFSR   OptOMP-LFSR via SOM

OptOMP-LFSR via EDUMS   OptMeanSubs-OMP-LFSR via SOM

Figure 36. Visual results of Vespa, $s = 3$

CHAPTER 5: CONCLUSION

LF is an imaging technique of capturing light rays from different locations and directions in order to obtain the 4D LF structure to produce 3D real-world scene. Due to hardware restrictions, LF views have low spatial resolution. Therefore, super-resolution methods can be used to improve the spatial resolution. However, recovering fine-details and removing blur are challenges because of ill-posed nature of this optimization problem. In this study, many solutions have been proposed with different tools to solve this optimization problem.

In this thesis, the well-known SISR and LFSR methods have been initially analyzed to better understand the nature of the problem and its solution proposals. During the research, some successful algorithms such as SR-LFBM5D (Alain and Smolic, 2018a) and (Türkan, Thoreau and Guillotel, 2013) have been inspiring works. It has been considered that the usage of texture details in the angular and spatial dimensions in the LF structure can be appropriate with their SR approaches. Thanks to this perspective, the exemplar-based LFSR methods are proposed in order to solve the problem by using patch-based and locally optimized approaches. By means of phase images and non-integer upsampling factors, the employment of effective local similarities is the main focus of the proposed LFSR methods. Moreover, LLE and OMP work to find patch approximations, and it is observed that MeanSubs-OMP provides HR images contained sharper and cleaner views.

The proposed algorithms are compared with several well-known benchmark studies. The comprehensive statistical and visual evaluation provides an inference that the proposed methods yield competitive performance. In particular, the method called *OptMeanSubs-OMP-LFSR via SOM* can be defined as a novel LFSR method to obtain superior performance on low disparity LF images.

The main disadvantage of the proposed methods is that the framework cannot produce high-quality images when the input images contain fine-detailed contents. In addition, during the study, the proposed approaches have been tested on different LF datasets. These datasets have high disparity between LF SAIs, and it is observed that the main exemplar-based approach may not be sufficient to eliminate blur artifacts. This

problem can simply be solved by estimating the blur kernel, deconvolving the image with the estimated kernel and applying a more sensitive neighbor-search method.

Additionally, the developed algorithms can be incorporated into NN-based or GAN-based frameworks to prevent computational complexity and extend their usage. With GPU processors or parallel processing, the computation time can also be remarkably reduced.

REFERENCES

Adelson, E.H. and Bergen, J.R. (2020) *The plenoptic function and the elements of early vision*, Computational Models of Visual Processing, pp. 3–20.

Alain, M. and Smolic, A. *Light field denoising by sparse 5D transform domain collaborative filtering. Proceedings of the IEEE International Workshop on Multimedia Signal Processing.* Luton, United Kingdom. 26-28 October 2017.

Alain, M. and Smolic, A. (2018a) *Light field super-resolution via LFBM5D sparse coding. Proceedings of the IEEE International Conference on Image Processing.* Athens, Greece. 07-10 October 2018.

Alain, M. and Smolic, A. (2018b) *Light Field Super-Resolution via LFBM5D Sparse Coding* [Online]. Available at: https://v-sense.scss.tcd.ie/research/light-fields/light-field-super-resolution-via-lfbm5d-sparse-coding/. (Accessed: 11 January 2023).

Bartholomew, D.J. (2010) *Principal components analysis. International Encyclopedia of Education*, pp. 374–377.

Boominathan, V., Mitra, K. and Veeraraghavan, A. *Improving resolution and depth-of-field of light field cameras using a hybrid imaging system. Proceedings of the IEEE International Conference on Computational Photography.* Santa Clara, California, USA. 02-04 May 2014.

Canny, J. (1986) *A computational approach to edge detection*, IEEE Transactions on Pattern Analysis and Machine Intelligence, Vol. PAMI-8(6), pp. 679–698.

Davis, G., Mallat, S. and Avellaneda, M. (1997) *Adaptive greedy approximations*, Constructive Approximation, Vol. 13(1), pp. 57–98.

Egiazarian, K. and Katkovnik, V. *Single image super-resolution via BM3D sparse coding Department of Signal Processing. Proceedings of the European Signal Processing Conference.* Nice, France. 31 August-04 September 2015.

Farrugia, R.A., Galea, C. and Guillemot, C. (2017) *Super resolution of light field images using linear subspace projection of patch-volumes*, IEEE Journal on Selected Topics in Signal Processing, Vol. 11(7), pp. 1058–1071.

Freedman, G. and Fattal, R. (2011) *Image and video upscaling from local self-examples,* ACM Transactions on Graphics, Vol. 30(2). pp. 1-11.

Glasner, D., Bagon, S. and Irani, M. *Super-resolution from a single image. Proceedings of the IEEE International Conference on Computer Vision.* Kyoto, Japan. 29 September – 02 October 2009.

He, K., Sun, J. and Tang, X. (2013) *Guided Image Filtering*, IEEE Transactions on Pattern Analysis and Machine Intelligence, Vol. 35(6), pp. 1397–1409.

Kay, S.M. (1993) *Fundamentals of Statistical Signal Processing: Estimation Theory*. Prentice Hall.

Kohonen, T. (1990) *The self-organizing map*, Proceedings of the IEEE, Vol. 78(9), pp. 1464–1480.

Matysiak, P., Grogan, M., le Pendu, M., Alain, M., Zerman, E. and Smolic, A. (2020) *High quality light field extraction and post-processing for raw plenoptic data*, IEEE Transactions on Image Processing, Vol. 29, pp. 4188–4203.

Mitra, K. and Veeraraghavan, A. *Light field denoising, light field superresolution and stereo camera based refocussing using a GMM light field patch prior. Proceedings of IEEE Computer Society Conference on Computer Vision and Pattern Recognition Workshops*. Providence, Rhode Island, USA. 16-21 June 2012.

Ng Ren (2006) *Digital light field photography*. Doctoral Thesis. Stanford University.

Pati, Y.C., Rezaiifar, R. and Krishnaprasad, P.S. *Orthogonal matching pursuit: recursive function approximation with applications to wavelet decomposition. Proceedings of 27th Asilomar Conference on Signals, Systems and Computers*. Pacific Grove, California, USA. 01-03 November 1993.

le Pendu, M., Jiang, X. and Guillemot, C. (2018) *Light Field Inpainting Propagation via Low Rank Matrix Completion,* IEEE Transactions on Image Processing, Vol. 27(4), pp. 1981–1993.

Peng, K.S., Lin, F.C., Huang, Y.P. and Shieh, H.P.D. *Efficient super resolution using edge directed unsharp masking sharpening method. Proceedings of the IEEE International Symposium on Multimedia.* Anaheim, California, USA. 09-11 December 2013.

Rerabek, M. and Ebrahimi, T. *New light field image dataset. International Conference on Quality of Multimedia Experience.* Lisbon, Portugal. 06-08 June 2016.

Rodríguez-Gironés, M.A. and Ruiz, A. (2016) *toBeeView: a program for simulating the retinal image of visual scenes on nonhuman eyes*, Ecology and Evolution, Vol. 6(21), pp. 7892–7900.

Rossi, M. and Frossard, P. (2018) *Geometry-consistent light field super-resolution via graph-based regularization*, IEEE Transactions on Image Processing, Vol. 27(9), pp. 4207–4218.

Roweis, S.T. and Saul, L.K. (2000) *Nonlinear dimensionality reduction by locally linear embedding*, Science, Vol. 290(5500), pp. 2323–2326.

Türkan, M., Thoreau, D. and Guillotel, P. *Optimized neighbor embeddings for single-image super-resolution*. Proceedings of the *IEEE International Conference on Image Processing*. Melbourne, Victoria, Australia. 15-18 September 2013.

Wang, Y., Liu, F., Zhang, K., Hou, G., Sun, Z. and Tan, T. (2018) *LFNet: A Novel Bidirectional Recurrent Convolutional Neural Network for Light-Field Image Super-Resolution*, IEEE Transactions on Image Processing, Vol. 27(9), pp. 4274–4286.

Yang, J., Wright, J., Huang, T.S. and Ma, Y. (2010) *Image super-resolution via sparse representation*, IEEE Transactions on Image Processing, Vol. 19(11), pp. 2861–2873.

Yoon, Y., Jeon, H.G., Yoo, D., Lee, J.Y. and Kweon, I.S. *Learning a Deep Convolutional Network for Light-Field Image Super-Resolution*. *Proceedings of the IEEE International Conference on Computer Vision Workshop*. Santiago, Chile. 07-13 December 2015.

Yoon, Y., Jeon, H.G., Yoo, D., Lee, J.Y. and Kweon, I.S. (2017) *Light-field image super-resolution using convolutional neural network*, IEEE Signal Processing Letters, Vol. 24(6), pp. 848–852.